

The local structure organization and dynamics in lithium borate ionic liquids using molecular dynamics simulation

Volodymyr Koverga and Anh T. Ngo

Department of Chemical Engineering, University of Illinois Chicago, Chicago, IL 60608, United States
Materials Science Division, Argonne National Laboratory, Lemont, IL 60439, United States

Abstract

Despite significant progress in the development of lithium-ion batteries, the majority still rely on electrolytes based on organic solvents. However, single-ion conducting electrolytes offer a promising alternative by mitigating overpotential at the electrode and, thus, increasing the device's lifespan. In a recent study, Guzmán-González *et al.* (*Adv. Energy Mater.*, 2022, 2202974) presented a novel approach to designing a new class of lithium ionic liquids, based on tetracoordinated boron atoms with oligoethylene glycol groups and different fluorinated electron-withdrawing groups. To gain insights into the structural and dynamic aspects underlying the high ionic conductivity of these electrolytes, molecular dynamics simulations were employed. Our results establish a relationship between the variation in ionic conductivity and the extent of uncorrelated motion among the counterions. This phenomenon was explained by differences in the rate of ion coordination dynamics.

Introduction

Since the first commercial lithium-ion batteries (LIBs) hit the market in the early 1990s, their development has transcended the realm of portable electronics. Their inherent features, including high specific capacity, voltage, lack of memory effect, excellent cycling performance, minimal self-discharge, and wide temperature range of operation,[1, 2] make them superior to other energy storage systems in the battery market today. Nevertheless, as material advancements approach their limits, the escalating demand for more cost-effective and high-performance devices necessitates a more rational approach in the development of the new generation of LIBs.[3]

In this context, electrolyte design is a fundamental challenge in battery electrochemistry.[4] Apart from the well-known requirements of electrolytes for conventional LIBs, such as high conductivity, chemical and electrochemical stability against the electrodes, low flammability, and environmental sustainability, the electrolytes must also prevent the formation of lithium dendrites by forming a passivating solid electrolyte interphase towards the metal anode.[5] Most current commercial LIBs use liquid

electrolytes based on volatile and flammable organic carbonate solvents, which can easily undergo drastic degradation processes.[6] Moreover, as a result of the ion-solvent imbalance in these electrolytes a formation of the concentration gradient essentially contributes to the LIB performance. Latter is explained by the high solvation of lithium in carbonate electrolytes leading to relatively low transference number of lithium (typically 0.35-0.40)[7] and high negative space charge due to the anion motion. Therefore, for the increasing of lithium transference number, ideally up to unit,[8] it is necessary to make a step forward in the development of solvent free/single-ion electrolytes.

Among the previously reported efforts to improve transference number by using electrolytes based on the metal-organic framework, polymers/polyanions, highly concentrated solutions or deep eutectic solvents, ionic liquids (ILs) were found to be the most promising candidate on this role due to their non-flammability, low vapor pressure, high thermal and electrochemical stability, and contains the charge-balanced anions and cations.[9] Incorporating of ILs as an electrolyte media in LIBs, however, hindrance the Li mobility due to the naturally high viscosity of ILs coupled with the presence of another larger cation in solution.[10] To reduce a high viscosity, ILs commonly admixing with organic electrolytes (or their mixtures), making the electrolyte more conducive via the solvation of Li^+ ions and the dissociation of lithium salts. As a result, the ion conductivity increased from 10^{-3} to 10^{-2} S cm^{-1} , [11] while the lithium salt concentration polarization persisted in the electrolyte due to the low transference number.

To completely suppress concentration polarization, a solvent-isolated lithium salts that (similar to common ILs) themselves are liquids at room temperature, were introduced as an alternative electrolyte in LIBs. Only a few such lithium ILs (LILs) exist today, based on lithium salts of aluminates and borates and lithium coordinating ether ligands with electron-withdrawing groups, which can reduce the anionic basicity and dissociate the cations from the anionic centers, respectively. The first generation of $\text{Li}^+\text{Al}(\text{OR})_4^-$ LILs was introduced by Fujinami and Buzoujima[12] that containing, where R represents two oligoether groups and CF_3CO_2 , CF_3SO_3 , $(\text{CF}_3\text{SO}_2)_2\text{N}$ or C_6F_5 were chosen as electron-withdrawing groups. They found that enhancement of the ionic conductivity (up to 10^{-4} S cm^{-1} at 40 °C) in these electrolytes is achieved by degree of salt dissociation which is ascribed to electron withdrawing ability of the groups anchored onto $\text{Al}(\text{OR})_4^-$ center. Moreover, the relatively high transference number is mainly associated with incorporation of short-length oligoether chains inducing the anion immobilization. In attempts to reduce the anion basicity and increase ion mobility, Watanabe *et al.*[13, 14] reported another type of borate-based LILs, where $\text{CH}(\text{CF}_3)_2$, C_6F_5 and CF_3CO are used as electron-withdrawing group along with Li^+ coordinating oligoether groups, so-called LiHFIP, LiPFP and LiTFA, respectively. Based on the detailed analysis of physicochemical properties of designed LILs, the authors noted a high viscosity as a main factor that limits ion conduction and increases the glass transition temperature. In the recent work of Shigenobu *et al.* reported that the borate-based LILs, among which LiHFIP and LiFTA were examined, induce concentration

polarization, which results in reduction of t_{Li} . Further, using molecular dynamics (MD) simulation approach Farhadian and Malek[15] tried to understand the nature of the low ion mobility in LiFTA. According to the reported results ion migration in the system can be described in terms of a hopping process, where the low ionic conductivity explained by the low rate of cation migration from one cage to another and the long lifetime of ion pairs.[16]

Other works devoted to functionalization of $Li^+B(OR)_4^-$ paved the route for a further understanding of the chemistry of LILs and the crucial factors for its improvements. Particularly, Zygadło-Monikowska *et al.*[17] obtain a new structure by substituting one of the oligo(ethylene oxide) by butyl group. It was reported that the ionic conductivity of the resulting salts depends on the number of ethylene oxide units, where the highest conductivity of $2 \times 10^{-5} S cm^{-1}$ is shown by the salt with chain length containing three monomers. To gain insight about how the functionalization of LILs affecting on the ionic conductivity, Guzmán-González *et al.*[18] reported a design concept of series borate-based LILs with various electron-withdrawing groups and alkane substituents. These LILs showed high ionic conductivity values (higher than $10^{-4} S cm^{-1}$ 25 °C) and transference number of 0.4-0.5, as well as high compatibility with lithium-metal electrodes with stable polarization profiles. The authors emphasize the presence of balance between the electron-withdrawing capacity of the fluorinated groups, the solvating capacity of the ethoxide groups, and the interfacial compatibility of the stabilizing aliphatic groups that allow to achieve higher conductivity values.

Despite the obvious potential of the LIL systems mentioned above, to date there is a limited number of works describing them using atomistic level details. Therefore, in this paper we present our results on the effect of electron-withdrawing groups on the local structure organization and dynamics in the recently reported LILs[18] from the point of MD simulation approach (see Figure for molecular structure). Apart from the fact that the experimental data on the ion dynamics are already available for these LILs, we believe that the description of the structure and interionic interactions between in Li^+ and the various anions in the LILs will gain an impact for the molecular design of novel LILs with higher characteristics of the ion mobility and also for explaining previously reported experimental findings.

Computational details

For classical MD simulation, the seven LILs composing seven anions with various electron-withdrawing groups, namely hexafluoro-2-propanoxy (LIL2), hexafluoro-2-methyl-2-propanoxy(LIL4) and trifluoro-2-propanoxy (LIL6), were selected. The non-polarizable all-atomic OPLS(-AA), “Optimized Potentials for Liquid Simulations”, [19, 20] force field as available in GROMACS topology database, was utilized to adjust most of the intra- and interatomic potential parameters, describing covalent terms within bond stretching, angle bending and dihedral angle torsion along the covalent bond, and non-covalent terms

represented by the van der Waals interactions. The Lennard-Jones parameters for B–O were adopted from Wang *et al.*[21] and Li was taken from the work of Farhadian and Malek[15] (see Figure 2). The Coulomb interactions were described by the partial charges evaluated in the framework of CHELPG, “CHarges from ELectrostatic Potentials using a Grid-based method”,[22] molecular electrostatic potential scheme using MP2/6-31++G(d, p) level of theory for the set of LIL’s ion pairs geometries, preliminary optimized in HF/6-31G(d) as available in Gaussian code, v16.[23] To boost the ion dynamics the Lennard-Jones parameters were modified, particularly, ϵ parameters were reduced for Li and H atoms ($\epsilon_{\text{Li}} = 0.2906$ and $\epsilon_{\text{H}} = 0.0255$ kJ mol⁻¹) to reduce the energetics in the interactions between the counterions and between the ethoxide group of the anion, respectively.

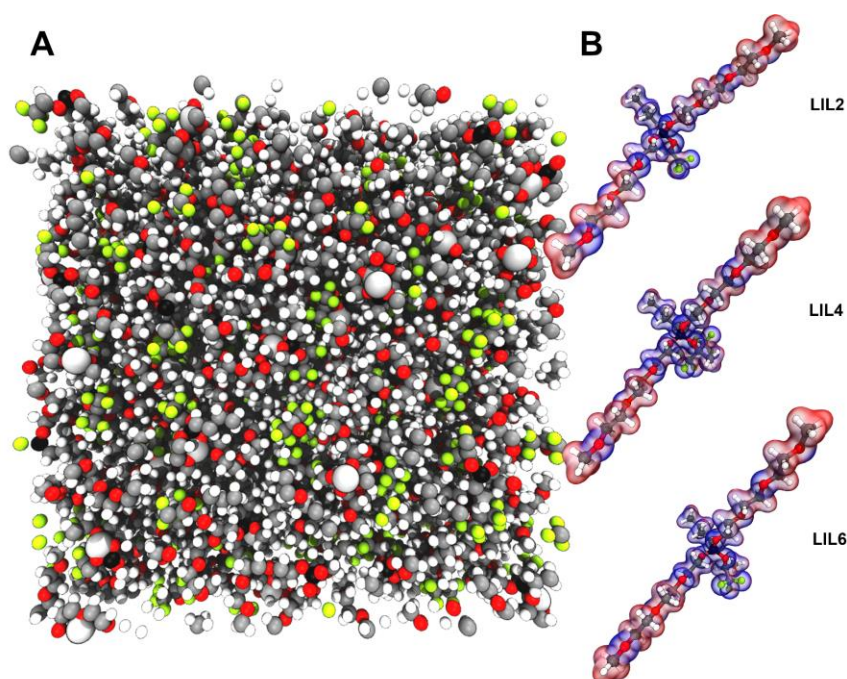


Figure 1. A) Illustration of the equilibrated MD cell for LIL system, B) molecular structure of the anions composing LILs, optimized in gas phase by means of *ab initio* calculations, and their electrostatic potential surface map. Blue, white and red color correspond to ESP varying from minimum to maximum level of 78.76 kJ mol⁻¹. Color code for elements: white – hydrogen, silver – lithium, black – boron, grey – carbon, red – oxygen, yellow – fluorine.

Optimized geometries were additionally checked to be in true minima by the absence of imaginary frequencies in the corresponding vibration spectra. Missing in database intraatomic potentials (except B–O and O–B–O that was taken from literature[21]) for atoms covalently bonded to central B atom of the anion were reparametrized using relaxed potential energy scan concept, *r*PES. To speed up the calculations all the LIL geometries were reduced by two ethylene oxide units from each side and reoptimized in the gas

phase using the same level of theory as for the full geometries. Next, a series of 10 scans was conducted to evaluate stretching and bending parameters using a step of 0.004 nm and 0.4°, respectively. For torsion potentials 18 scans with a step of 10° were implemented. The obtained in this way *r*PES profiles were averaged over all the degrees of freedom of the same nature and subsequently fitted by suitable polynomials according to OPLS-AA analytical expression of the potential energy adopted for GROMACS environment.

$$U = \sum_{bond} \frac{k_r}{2} (r_i - r_0)^2 + \sum_{angle} \frac{k_\theta}{2} (\theta_i - \theta_0)^2 + \sum_{dihedral} \sum_{n=0}^5 C_n (\cos(\phi - 180))^n$$

where U is a sum over the internal terms as a function of atomic coordinates represented by bond distances (r), angles (θ), and dihedrals (ϕ); The parameters k_n and C_n are the respective force constants and the variables.

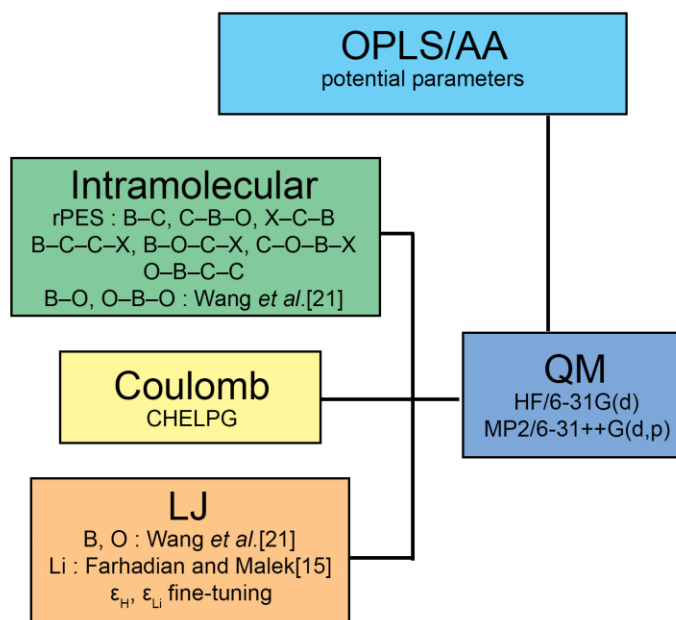


Figure 2. Flowchart describing the protocol for setting potential model parameters: most of the potential parameters were adapted from OPLS/AA, followed by relaxed potential energy surface scan to derive the missing intramolecular parameters involving central B atom; partial charges were analyzed using quantum-chemical approach, and ϵ for H and Li were tuned to reproduce experimental ionic conductivity.

The initial coordinates of 256 ion pairs were generated using Packmol code[24] and placed into the orthorhombic supercell of 10 × 10 × 10 nm with three-dimensional periodic boundary conditions. Such system size was selected to avoid deleterious pressure fluctuations and to reduce the influence of the on

finite size effects on the electrostatic interactions during the equilibration stage, while a considerably larger box was taken to avoid the intermolecular clashes. All MD simulations were carried out using GROMACS, v2016.3.[25-30] Equations of motion were integrated using a leap-frog algorithm with a time-step of 2 fs. The time-step selection was justified by utilization of C–H bonds constraints, which was achieved with LINCS, “LINear Constraint Solver”, algorithm.[31] The electrostatic long-range interactions within the cut-off range of 1.4 nm were accounted by the computationally efficient Particle Mesh Ewald algorithm,[32] using the same cut-off distance for the real-space component. The 12-6 Lennard-Jones interactions were treated by the conventional shifted force technique with a switch region between 1.2 and 1.3 nm. Cross interactions between different atom types were derived using standard Lorentz-Berthelot combination rules.

The simulation protocol implied a stepwise equilibration procedure, followed by sampling the coordinates for the analysis. Thus, each system was, firstly, minimized using steepest descent algorithm with the default convergence criterion, next, a series of equilibration steps in an isothermal-isobaric (npT) and canonical (nVT) ensembles was conducted to reach experimental density of $\sim 1.021 \pm 0.006 \text{ g cm}^{-3}$ [18] and relax the LIL geometry:

1. 0.1 ns of npT compression at 100 bar and 373 K using Berendsen thermostat and barostat[33] with coupling constants, τ , of 3×10^{-4} and 5×10^{-4} ns;
2. 0.5 ns of npT compression at 100 bar and 373 K;
3. 0.5 ns of npT compression at 100 bar and 373 K using velocity rescaling thermostat ($\tau_T = 10^{-4}$)[34] and Berendsen barostat;
4. 1 ns nVT heating at 603 K;
5. 1 ns of npT compression at 100 bar and 298 K;
6. 5 ns of npT compression at 1 bar and 298 K using Parrinello-Rahman barostat to estimate equilibrium density;[35]
7. 1 ns of nVT production using Nose-Hoover thermostat[36-38] to collect the coordinates with the total number of 10000 frames for the analysis of the local structure organization;
8. 10 ns of nVT to collect the coordinates for the analysis of ion dynamics

The analysis electrostatic potential map was conducted using Muliwfn code, v3.8,[39], local structure analysis discussed in this work was performed using TRAVIS, “TRajjectory Analyzer and VISualizer” code, vJuly 29, 2022[40, 41], and analysis of the ion dynamics (except dimer existence autocorrelation function), was conducted using GROMACS tools. Particularly, self-diffusion coefficient was obtained by the with Einstein equation by linear fitting of the center-of-mass mean-square displacement of the ions involved in LIL as a function of simulated time:

$$D = \frac{1}{6} \lim_{t \rightarrow \infty} \frac{d}{dt} \langle \Delta \mathbf{r}(t)^2 \rangle$$

where $\langle \Delta \mathbf{r}(t)^2 \rangle$ is an ensemble-averaged difference between vector position of species at time t . Ionic conductivity was estimated using the Einstein-Helfand relation by linear fitting of the collective translational dipole moment of ionic motion:

$$\sigma = \frac{1}{6k_BVT} \lim_{t \rightarrow \infty} \frac{d}{dt} \langle \Delta \mathbf{M}_J(t)^2 \rangle$$

where $\langle \Delta \mathbf{M}_J(t)^2 \rangle$ is an ensemble-averaged difference between vector position of N species with an effective net-charge q at time t . The final values of self-diffusion and ionic conductivity were estimated based of Fickian formalism, according to which $\langle \Delta \mathbf{x}(t)^2 \rangle \propto t^\beta$, where β was estimated using the equation (\mathbf{x} stands for \mathbf{r} or \mathbf{M}_J):

$$\beta = \frac{d \log \langle \Delta \mathbf{x}(t)^2 \rangle}{d \log t} = 1$$

Further, to estimate the degree of the ion uncorrelated motion (also known as Haven ratio), which measure the deviation of the collective ionic motion with respect to ideal one, where this motion is not counted, the ionic conductivity was analyzed by Nernst-Einstein equation:

$$\sigma_{NE} = \frac{Nq^2}{6k_BVT} (D_+ + D_-)$$

To further study the ion transport mechanism, self-part of the van Hove correlation function was examined with equation:

$$G_s(r, t) = \frac{1}{N} \sum_{i=1}^N \langle \delta(\mathbf{r} - |\mathbf{r}_i(t) - \mathbf{r}_i(0)|) \rangle$$

where N is the total number of particles in the system, $\mathbf{r}_i(t)$ is the position of the i^{th} particle at the given time t , and δ represents the Kronecker delta; following examination of the correlated motion of the particles,

using the collective van Hove correlation function. The information about the coordination dynamics of the ions was archived by examination of dimer existence autocorrelation function, determined using cutoff distance from the minimum in radial distribution function, describing the interactions between atom i and j of the cation and anion, respectively:

$$\tau = 2 \int_0^{\infty} \left(\frac{1}{N^2} \sum_{i=1}^N \sum_{j=1}^N \int_0^{\infty} \beta_{ij}(t) \beta_{ij}(\tau) dt \right) d\tau$$

Results and discussion

As a preliminary step in the analysis of the simulated LILs, the theoretical density was examined against the experimental one for LIL2. Nevertheless, owing that the density in such systems does not vary significantly, we expected the negligible variation from system to system. Following the obtained results, the maximum deviation was found of 16% for LIL2 (1.1883 g cm⁻³) and LIL4 (1.1877 g cm⁻³), and 8% for LIL6 (1.1058 g cm⁻³), respectively. This suggests a fairly accurate predictive ability of the modified potential model parameters in terms, at least, of the local structure organization analysis.

Next, the ionic conductivity was examined against the reported experimental measurements. One needs to stress that tuning of the potential model parameters was employed based on LIL6, and, assuming the transferability of the empirical force field, the deviation supposed to be the same for all the studied systems. In fact, we found a relatively small difference in conductivity for LIL6 (~18%), while for LIL2 and LIL4 it is essentially larger (~50%). Nevertheless, the obtained trend is well corroborated with the measurements, showing a higher ion conduction for LIL6 and lower for LIL2 and LIL4, respectively (Figure 3). Such behavior was previously explained by the features of the electronic structure in LILs, where the level of electronic delocalization in the electron-withdrawing group along with size of the molecular structure offer a higher rate of ion dissociation. To make a step toward the understanding of this phenomena, the self-diffusion coefficient for LIL's cation and anion was analyzed. According to the obtained results, despite the bulky anion, it exhibits a higher mobility compared to Li⁺. Such behavior was also observed in previously published works on ILs[42]. We found that, depending on the LIL, the difference between cation and anion motion is increasing in the row: LIL6 (~19%) > LIL2 (~25%) > LIL4 (~27%). We assume that this trend may be related to the different coordination ability of cation with respect to the anion on one hand, as well as with a different extent of the correlation between the ions. This assumption was addressed by estimating a Haven's ratio, defined as $H = \sigma/\sigma_{NE}$. The higher value of H found for LIL6 ($H = 0.13$) implies a lower in the correlated motion between oppositely charged ions and also

lower anticorrelated motion between ions of the same charge, where on opposite situation observed for LIL2 and LIL4, with H values of 0.095 and 0.092, respectively.

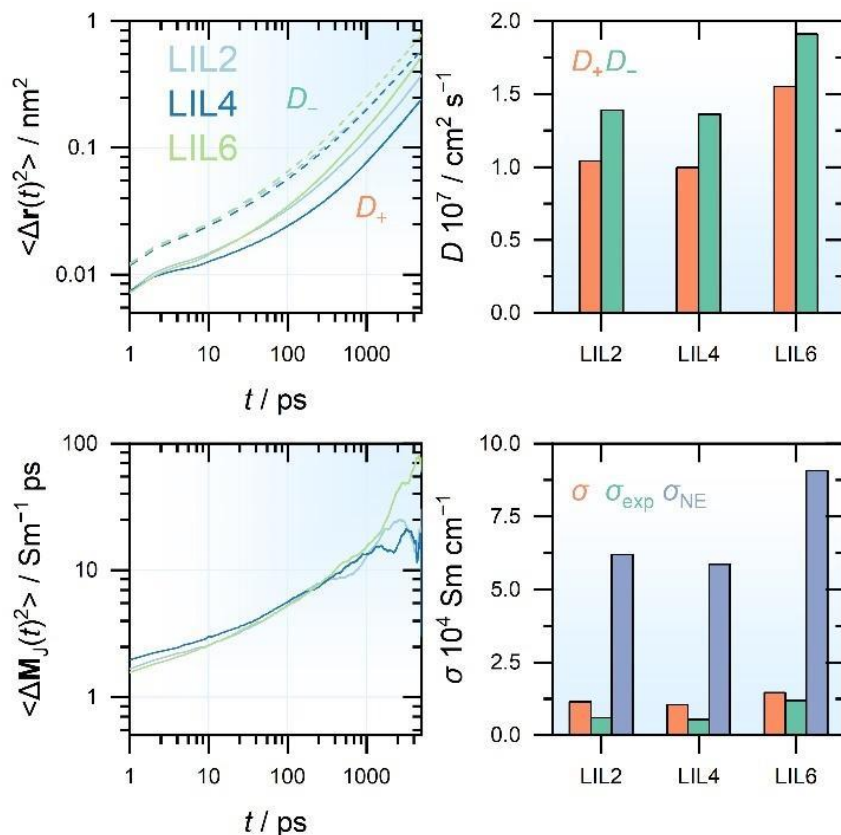


Figure 3. Illustration of mean-square displacement, $\langle \Delta \mathbf{r}(t)^2 \rangle$, and translational part of the dipole moment, $\langle \Delta \mathbf{M}_J(t)^2 \rangle$, of the ions in studied LIL system, along with self-diffusion coefficient, D , estimated at the time > 1.5 ns and ionic conductivity estimated in the time-range between 0.25 and 1.2 ns against the experimental results.

To understand the difference in the ion transport behavior occurred in different LILs, the van Hove correlation function was analyzed in terms of Li^+ self-part, describing the translational distance of Li^+ ions on the time interval, as well as between different cations, describing the correlation of such translational distance. Based on the analyzed $G_S(r_{\text{Li}}, t)$ plots for the different LILs (Figure 4), one can notice a general tendency of a short-range translation of Li^+ at low time intervals, followed by extension into the larger distances at larger times. Moreover, the position of the first peak in corresponding plots is shifted towards the larger distances, which is accompanied by a distortion of the Gaussian-like shape of the plot. Apart from this trend, all the LILs feature different extensions of the Li^+ distribution at the same time intervals. Particularly, for all the LILs at the time intervals > 1200 ps, the lower translation distance of the cation was found for LIL4 and LIL2 compared to LIL6, whereas this difference becomes more noticeable at $t = 10000$

ps – 1.73, 1.84 and 1.93 nm, respectively. Another characteristic feature is the formation of the second peak or shoulder for the large time intervals at larger Li^+ displacements. Tracking this time evolution, the formation of the second peak is clearly seen for LIL4 ($t > 1600$ ps), which is characterized by lower ion transport properties, where the formation of such a peak for LIL2 is barely seen for $t = 10000$ ps. The overall changes observed in $G_S(r_{\text{Li}}, t)$ for the considered LILs at different time intervals and translation distances may be interpreted in terms of the ion hopping mechanism, where the Li^+ transport is reduced inside the caged structure formation by the counterion. Thus, the Gaussian-like distribution at short time intervals indicates a Li^+ translation by a diffusion motion, however a formation of the shoulders at larger distances (and deviation from the Gaussian shape) and time intervals indicates hopping motion along the diffusive one.

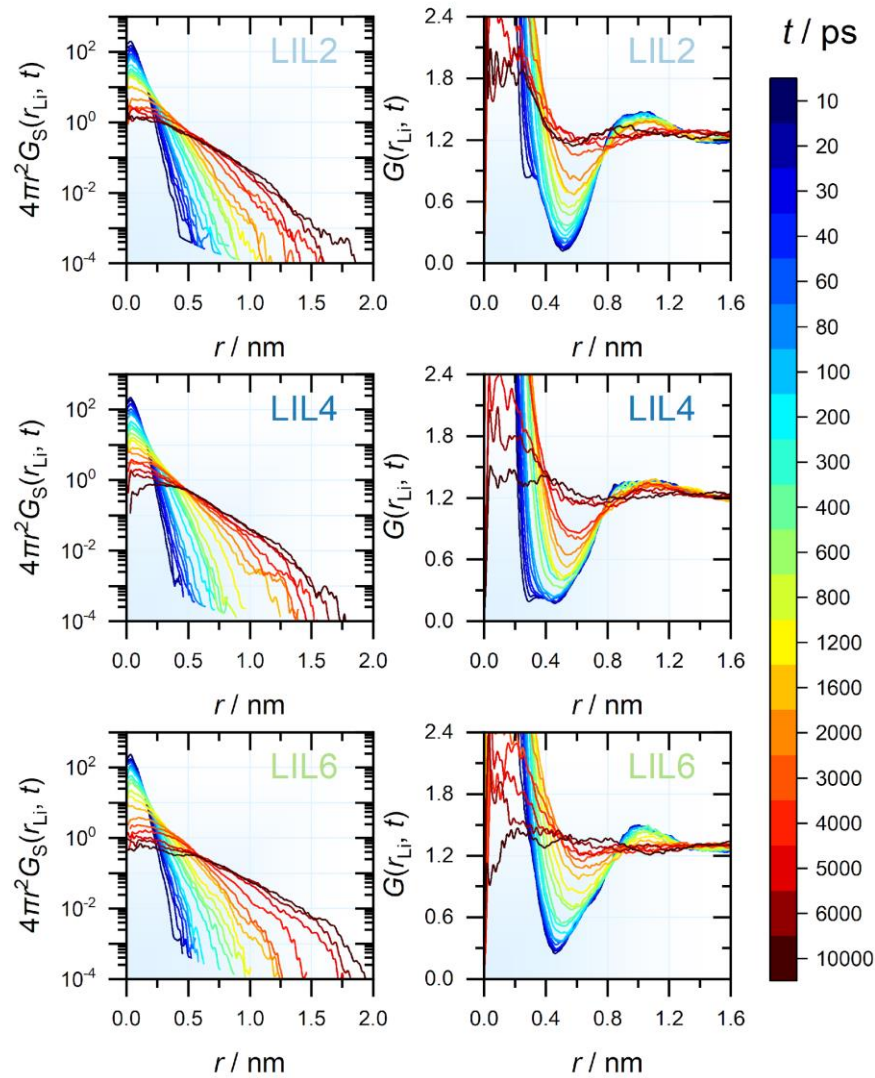


Figure 4. Illustration of time evolution of the self-part, $G_S(r, t)$, and collective, $G(r, t)$, van Hove correlation function for Li^+ in LIL2, LIL4 and LIL6.

To cover the entire pattern of Li^+ transport in different LILs, it is also important to take into account the correlation motion, which, as noted above, largely determines the ionic conductivity. As can be seen from the results obtained for $G(r_{\text{Li}}, t)$, a general tendency shows that the Li^+ profiles a first peak at $r = 0$, and then, passing through the minima at *ca* 0.4 nm, form the second peak at 0.9-1.05 nm. Similarly to $G_{\text{S}}(r_{\text{Li}}, t)$ profiles, the increasing of time intervals shifts the peak position toward the larger distances, gradually reducing the intensity. The decreasing in the intensity implies a diffusive motion of cation toward the reference Li^+ vacancy position. The higher intensity of the peak at $r = 0$ (LIL2 > LIL4 > LIL6) indicates a higher correlated motion, *i.e.*, diffusive motion of Li-ion accompanied by the hopping with respect to the reference one.

As a second step of the analysis, the radial distribution function, $g(r)$, was employed to examine the local environment around Li^+ . As it might be seen from Figure 5, the resulting curves, reflecting the pair distances between $\text{Li}\cdots\text{B}$ and $\text{Li}\cdots\text{O}$, exhibit a well-defined first peak of similar shape, accompanied by a broad solvation shell. For most of the systems, the position of the first peak of the $g(r_{\text{Li}\cdots\text{O}})$ occurs around 0.16 nm, while the peak $g(r_{\text{Li}\cdots\text{B}})$ located slightly further at 0.22 nm. The only exception was found for LIL6, where the $g(r_{\text{Li}\cdots\text{B}})$ distribution show a forked peak, while $g(r_{\text{Li}\cdots\text{O}})$ located at slightly lower distances of 0.15 nm. Despite the relatively high positive charge of boron atom, it can be inferred that the position of the considered radial distributions demonstrates a preferential localization of Li^+ around B–O bond of the LIL anion, rather along the ethoxide groups. These findings align with LIL ion pairs optimized through *ab initio* calculations in the gas phase. In this context, the $\text{Li}\cdots\text{B}$ distances were determined to be approximately 0.22-0.25 nm, while for $\text{Li}\cdots\text{O}$ covalently bonded to the boron atom, the minimum distance was found to be 0.18-0.21 nm. Further examination of Li^+ solvation by other oxygen atoms of ethoxide group revealed slightly larger distances of about 0.20-0.22 nm. Nevertheless, position of Li^+ with respect to other oxygen atoms is hard to recognize with generalized $g(r)$, due to the similarities in peak positions, aside from intensity differences. To address this issue, a nearest neighbors' approach[43] was additionally employed. According to the obtained results, the $\text{Li}\cdots\text{B}$ distance ranged from 0.22-0.24 nm (LIL6 < LIL2 < LIL4) and the closest oxygen atom, at distances 0.17-0.22 nm, belongs to B–O bond and the first ethoxide unit (LIL6 < LIL2 ~ LIL4). The participation of the second and third units in the solvation process was minimal, with distances of 0.23-0.32 nm and 0.30-0.46 nm, respectively. These observations are similar to ones reported by Farhadian and Malek[15], where oxygen atoms of B–O bond attached to ethoxide group exhibited a higher probability of the interaction with Li^+ compared to oxygen attached to electron-withdrawing group in LiTFA.

To obtain additional information on the Li^+ solvation environment and its coordination ability, *cn*, the integration of the $g(r_{\text{Li}\cdots\text{O}})$ up to the first minimum at approximately 0.23-0.24 nm was conducted. Since the oxygen atoms of two distant ethoxide units do not participate in Li^+ solvation, the analysis considered

only the closest oxygen atoms. For all the LILs, it was observed that the Li^+ coordination ability generally follows the same trend as reported for ionic conductivity: $\text{LIL6} (cn = 2.01) < \text{LIL2} (2.51) < \text{LIL4} (2.78)$. This emphasizes the fact that higher Li^+ solvation leads to a decrease in ionic conductivity.

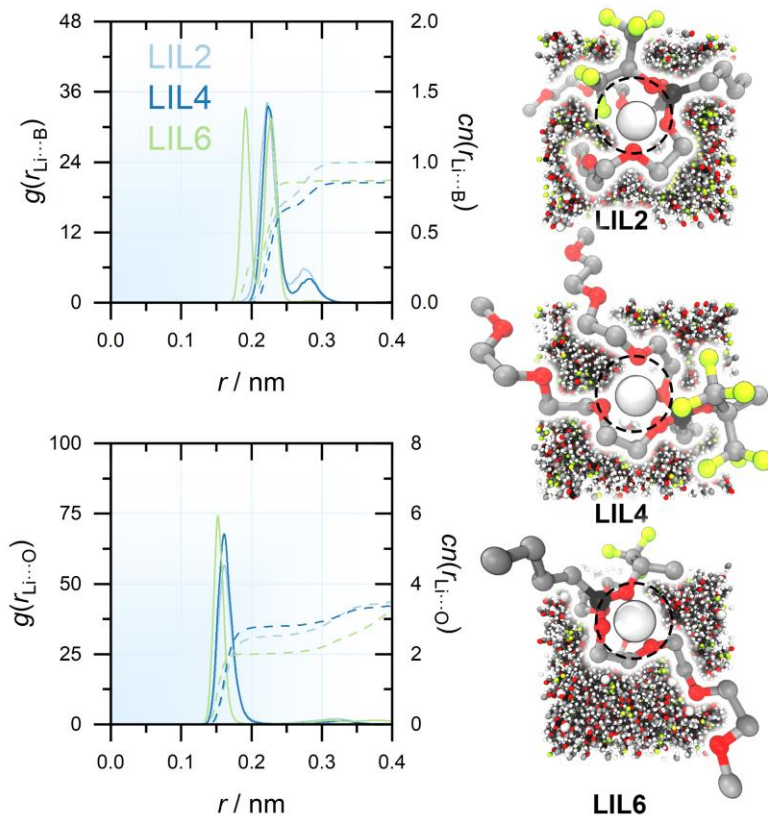


Figure 5. Illustration of the Li^+ solvation environment for the set of LILs, obtained using radial distribution function, $g(r)$, and running coordination number, cn , analysis for the $\text{Li}\cdots\text{B}$ and $\text{Li}\cdots\text{O}$ atomic pairs in a proximity to the central boron atom $-\text{B}-\text{O}-\text{CH}_2$ and $\text{CH}_2-\text{O}-\text{CH}_2$, along with Li^+ solvation structure for LIL2, LIL4 and LIL6. Dashed black line represents the border of the solvation shell of 0.22-0.24 nm, determined by the interaction between Li and oxygen of the first ethoxide unit; hydrogen atoms are hidden for the sake of simplicity.

To link the results on the local structure organization with ion dynamics, it is important to estimate the time during which cation remains coordinated by the anion. For this purpose, the ion lifetime was analyzed in LILs. Thus, it was found that the shorter lifetime is inherent for LIL6 (8.74 ns), rather than LIL4 (10.5 ns) and LIL2 (10.4 ns). Such tendency implies that higher ion dissociation occurs for LIL6 as a result of lower coordination ability of Li^+ to LIL6 anion, and therefore in promote a higher ion mobility and conductivity.

Conclusions

In this work, we examined physical properties along with structural and microdynamics aspects in three lithium ionic liquids (LILs), differing by electron-withdrawing group, recently synthesized by Guzmán-González *et al.*[18] We established the relationship between the features of ionic motion and the local structural organization with respect to the geometry of these LILs. Our findings reveal that the higher ionic conductivity observed in LIL6 and LIL2 is attributed to a reduced correlation in anion movement, thereby enhancing ionic mobility. Additionally, this phenomenon was explained by the analysis of van Hove correlation function, both self and collective. Thus, for LIL6 the Li⁺ transport mechanism is generally characterized by diffusive motion, while in LIL2 and LIL4 the cation diffusion is reduced due to the formation of the caged structure by the counterion. The diffusive motion of Li-ion in these LILs is accompanied by the hopping with respect to the reference one, which leads to a decrease in ionic conductivity. The analysis of the local structure indicates that despite comparable interionic interactions, the coordination ability of the cation with respect to the anion varies and follows the order of ionic conductivity: LIL6 < LIL2 < LIL4. Additionally, our investigation of coordination dynamics demonstrates a consistent trend in the rate of ion dissociation. Overall, this work sheds light on the intricate relationship between physical properties, structural aspects, and microdynamics in these lithium ionic liquids, offering valuable insights into their behavior and potential applications.

Acknowledgments

This work was supported by the Assistant Secretary for Energy Efficiency and Renewable Energy, Office of Vehicle Technologies of the US Department of Energy, through the Battery Materials Research (BMR) program. We gratefully acknowledge the computing resources provided on Bebop, a high-performance computing cluster operated by the Laboratory Computing Resource Center at Argonne National Laboratory.

References

1. Manthiram, A., *An Outlook on Lithium Ion Battery Technology*. ACS Central Science, 2017. **3**(10): p. 1063-1069.
2. Kim, T., et al., *Lithium-ion batteries: outlook on present, future, and hybridized technologies*. Journal of Materials Chemistry A, 2019. **7**(7): p. 2942-2964.
3. Frith, J.T., M.J. Lacey, and U. Ulissi, *A non-academic perspective on the future of lithium-based batteries*. Nature Communications, 2023. **14**(1): p. 420.

4. Quartarone, E. and P. Mustarelli, *Review—Emerging Trends in the Design of Electrolytes for Lithium and Post-Lithium Batteries*. Journal of The Electrochemical Society, 2020. **167**(5): p. 050508.
5. Xing, J., et al., *A Review of Nonaqueous Electrolytes, Binders, and Separators for Lithium-Ion Batteries*. Electrochemical Energy Reviews, 2022. **5**(4): p. 14.
6. Cao, C., Y. Zhong, and Z. Shao, *Electrolyte Engineering for Safer Lithium-Ion Batteries: A Review*. Chinese Journal of Chemistry, 2023. **41**(9): p. 1119-1141.
7. Valøen, L.O. and J.N. Reimers, *Transport Properties of LiPF₆-Based Li-Ion Battery Electrolytes*. Journal of The Electrochemical Society, 2005. **152**(5): p. A882.
8. Logan, E.R. and J.R. Dahn, *Electrolyte Design for Fast-Charging Li-Ion Batteries*. Trends in Chemistry, 2020. **2**(4): p. 354-366.
9. Yang, Q., et al., *Ionic liquids and derived materials for lithium and sodium batteries*. Chemical Society Reviews, 2018. **47**(6): p. 2020-2064.
10. Liu, K., et al., *Ionic liquids for high performance lithium metal batteries*. Journal of Energy Chemistry, 2021. **59**: p. 320-333.
11. Agostini, M., et al., *Characteristics of a Graphene Nanoplatelet Anode in Advanced Lithium-Ion Batteries Using Ionic Liquid Added by a Carbonate Electrolyte*. Advanced Materials Interfaces, 2015. **2**(8): p. 1500085.
12. Fujinami, T. and Y. Buzoujima, *Novel lithium salts exhibiting high lithium ion transference numbers in polymer electrolytes*. Journal of Power Sources, 2003. **119-121**: p. 438-441.
13. Shobukawa, H., et al., *Preparation and transport properties of novel lithium ionic liquids*. Electrochimica Acta, 2004. **50**(2): p. 305-309.
14. Shobukawa, H., et al., *Ion transport properties of lithium ionic liquids and their ion gels*. Electrochimica Acta, 2005. **50**(19): p. 3872-3877.
15. Farhadian, N. and K. Malek, *Investigating the physicochemical and transport properties of LiTFA ionic liquids by molecular dynamics simulation*. Solid State Ionics, 2014. **268**: p. 162-168.
16. Watanabe, M., et al., *Application of Ionic Liquids to Energy Storage and Conversion Materials and Devices*. Chemical Reviews, 2017. **117**(10): p. 7190-7239.
17. Zygadło-Monikowska, E., et al., *Lithium conducting ionic liquids based on lithium borate salts*. Journal of Power Sources, 2010. **195**(18): p. 6055-6061.
18. Guzmán-González, G., et al., *Lithium Borate Ionic Liquids as Single-Component Electrolytes for Batteries*. Advanced Energy Materials, 2023. **13**(1): p. 2202974.

19. Jorgensen, W.L. and J. Tirado-Rives, *The OPLS [optimized potentials for liquid simulations] potential functions for proteins, energy minimizations for crystals of cyclic peptides and crambin*. Journal of the American Chemical Society, 1988. **110**(6): p. 1657-1666.
20. Jorgensen, W.L., D.S. Maxwell, and J. Tirado-Rives, *Development and Testing of the OPLS All-Atom Force Field on Conformational Energetics and Properties of Organic Liquids*. Journal of the American Chemical Society, 1996. **118**(45): p. 11225-11236.
21. Wang, Y.-L., et al., *Atomistic Insight into Orthoborate-Based Ionic Liquids: Force Field Development and Evaluation*. The Journal of Physical Chemistry B, 2014. **118**(29): p. 8711-8723.
22. Breneman, C.M. and K.B. Wiberg, *Determining atom-centered monopoles from molecular electrostatic potentials. The need for high sampling density in formamide conformational analysis*. Journal of Computational Chemistry, 1990. **11**(3): p. 361-373.
23. Bilgili, S., A. Atac, and F. Bardak, *Theoretical and experimental investigation of the spectroscopic features of and interionic interactions in 1-hexyl-3-methylimidazolium chloride, 1-hexyl-3-methylimidazolium tetrafluoroborate and 1-hexyl-3-methylimidazolium hexafluorophosphate ionic liquids*. Journal of Molecular Liquids, 2020. **301**: p. 112468.
24. Martínez, L., et al., *PACKMOL: A package for building initial configurations for molecular dynamics simulations*. Journal of Computational Chemistry, 2009. **30**(13): p. 2157-2164.
25. Berendsen, H.J.C., D. van der Spoel, and R. van Drunen, *GROMACS: A message-passing parallel molecular dynamics implementation*. Computer Physics Communications, 1995. **91**(1): p. 43-56.
26. Lindahl, E., B. Hess, and D. van der Spoel, *GROMACS 3.0: a package for molecular simulation and trajectory analysis*. Molecular modeling annual, 2001. **7**(8): p. 306-317.
27. Van Der Spoel, D., et al., *GROMACS: Fast, flexible, and free*. Journal of Computational Chemistry, 2005. **26**(16): p. 1701-1718.
28. Hess, B., et al., *GROMACS 4: Algorithms for Highly Efficient, Load-Balanced, and Scalable Molecular Simulation*. Journal of Chemical Theory and Computation, 2008. **4**(3): p. 435-447.
29. Pronk, S., et al., *GROMACS 4.5: a high-throughput and highly parallel open source molecular simulation toolkit*. Bioinformatics, 2013. **29**(7): p. 845-854.
30. Abraham, M.J., et al., *GROMACS: High performance molecular simulations through multi-level parallelism from laptops to supercomputers*. SoftwareX, 2015. **1-2**: p. 19-25.
31. Hess, B., et al., *LINCS: A linear constraint solver for molecular simulations*. Journal of Computational Chemistry, 1997. **18**(12): p. 1463-1472.
32. Darden, T., D. York, and L. Pedersen, *Particle mesh Ewald: An $N \cdot \log(N)$ method for Ewald sums in large systems*. The Journal of Chemical Physics, 1993. **98**(12): p. 10089-10092.

33. Berendsen, H.J.C., et al., *Molecular dynamics with coupling to an external bath*. The Journal of Chemical Physics, 1984. **81**(8): p. 3684-3690.
34. Bussi, G., D. Donadio, and M. Parrinello, *Canonical sampling through velocity rescaling*. The Journal of Chemical Physics, 2007. **126**(1): p. 014101.
35. Parrinello, M. and A. Rahman, *Polymorphic transitions in single crystals: A new molecular dynamics method*. Journal of Applied Physics, 1981. **52**(12): p. 7182-7190.
36. Hoover, W.G., A.J.C. Ladd, and B. Moran, *High-Strain-Rate Plastic Flow Studied via Nonequilibrium Molecular Dynamics*. Physical Review Letters, 1982. **48**(26): p. 1818-1820.
37. Nosé, S., *A unified formulation of the constant temperature molecular dynamics methods*. The Journal of Chemical Physics, 1984. **81**(1): p. 511-519.
38. Nosé, S., *A molecular dynamics method for simulations in the canonical ensemble*. Molecular Physics, 1984. **52**(2): p. 255-268.
39. Lu, T. and F. Chen, *Multiwfn: A multifunctional wavefunction analyzer*. Journal of Computational Chemistry, 2012. **33**(5): p. 580-592.
40. Brehm, M. and B. Kirchner, *TRAVIS - A Free Analyzer and Visualizer for Monte Carlo and Molecular Dynamics Trajectories*. Journal of Chemical Information and Modeling, 2011. **51**(8): p. 2007-2023.
41. Brehm, M., et al., *TRAVIS—A free analyzer for trajectories from molecular simulation*. The Journal of Chemical Physics, 2020. **152**(16): p. 164105.
42. Bedrov, D., et al., *Molecular Dynamics Simulations of Ionic Liquids and Electrolytes Using Polarizable Force Fields*. Chemical Reviews, 2019. **119**(13): p. 7940-7995.
43. Koverga, V.A., et al., *Distance Angle Descriptors of the Interionic and Ion–Solvent Interactions in Imidazolium-Based Ionic Liquid Mixtures with Aprotic Solvents: A Molecular Dynamics Simulation Study*. The Journal of Physical Chemistry B, 2019. **123**(28): p. 6065-6075.